

Cite this: *Chem. Sci.*, 2025, **16**, 10803

All publication charges for this article have been paid for by the Royal Society of Chemistry

## Atomic Ni-doped $\text{ZrO}_2$ with subnanometric Fe clusters for tandem C–C bond cleavage and coupling†

Xin Zhao,<sup>a</sup> Jie Wen,<sup>a</sup> Qian Qiang,<sup>bc</sup> Dawang Tang,<sup>a</sup> Fengliang Wang,<sup>a</sup> Ruiqi Fang,<sup>id</sup> \*<sup>a</sup> Changzhi Li<sup>bc</sup> and Yingwei Li<sup>id</sup> \*<sup>a</sup>

The sustainable valorization of lignin  $\beta$ -O-4 compounds into high-value natural products through one-pot tandem catalysis presents an urgent yet scientifically challenging frontier in biomass conversion. Herein, we report a mesoporous  $\text{Fe}_3@\text{Ni}_1\text{-ZrO}_2$  catalyst featuring subnanometric Fe–O clusters anchored on atomic Ni-doped  $\text{ZrO}_2$  nanosheets. This engineered architecture enables the one-pot tandem conversion of lignin  $\beta$ -O-4 segments to flavones under aerobic and base-free conditions, delivering 56.2% yield with a space-time yield (STY) of  $3.3 \text{ g g}_{\text{cat}}^{-1} \text{ h}^{-1}$  in continuous flow operation. Moreover, the system demonstrates exceptional substrate versatility through efficient conversion of diverse lignin  $\beta$ -O-4 dimers and substituted 2'-phenoxyacetophenones into bioactive flavones. Mechanistic investigations combining controlled experiments and density functional theory (DFT) calculations reveal a cooperative catalytic mechanism, *i.e.*,  $\text{ZrO}_2$  nanosheets mediate selective oxidative cleavage of C–C bonds in  $\beta$ -O-4 segments, and subnanometric  $\text{Fe}_3$  clusters activate aldol condensation of cleavage intermediates, while atomic Ni sites suppress competing pathways to govern the selectivity. This synergistic interplay within the  $\text{Fe}_3@\text{Ni}_1\text{-ZrO}_2$  framework establishes a robust catalytic microenvironment to enable a high-efficiency tandem process.

Received 23rd March 2025  
Accepted 14th May 2025

DOI: 10.1039/d5sc02215k  
[rsc.li/chemical-science](http://rsc.li/chemical-science)

## Introduction

Lignin is a major component of lignocellulosic biomass, constituting approximately 30% of organic carbon reserves on Earth.<sup>1–3</sup> As the largest and only renewable aromatic feedstock,<sup>4–7</sup> it features a complex and recalcitrant polymeric structure consisting of multiple methoxylated phenylpropane subunits interconnected by diverse C–O and C–C bonds ( $\beta$ -O-4, 5–5 linkages, *etc.*).<sup>8–12</sup> Typical lignin valorization strategies prioritize C–O bond cleavage to acquire various phenolic chemicals,<sup>13–18</sup> whereas C–C bond scission remains a formidable challenge due to high bond dissociation energies. In order to improve the overall atomic utilization efficiency and biorefinery economics, selective cleavage of the C–C bond has emerged as a critical frontier. The  $\beta$ -O-4 linkage is the most frequent motif in lignin and integrates both C–O and C–C bonds,<sup>19–23</sup> making it an ideal model system for elucidating

bond cleavage mechanisms and guiding lignin valorization, as demonstrated by recent elegant progress.<sup>24–27</sup>

Flavonoids are a class of plant-derived phenolic metabolites that exhibit potent antioxidant properties and versatile bioactivities against cancer, cardiovascular diseases, and aging.<sup>28–31</sup> Currently, flavonoid production relies predominantly on plant extraction,<sup>32</sup> yet low biosynthesis rates and limited natural abundance fail to meet escalating pharmaceutical demands. Consequently, efficient artificial synthesis of flavonoids from renewable resources is urgently needed but remains largely unexplored.<sup>33</sup> On account of the functionalized aromatic skeleton of lignin  $\beta$ -O-4 segments in the structure, they offer a structurally congruent feedstock for flavonoid synthesis, which is promising to achieve a value-added biorefinery concept. In order to realize this promising transformation, a multi-step process including two sections is required, *i.e.*,  $\beta$ -O-4 segment depolymerization to aromatic monomers and a coupling reaction to assemble flavonoid oxygen-containing heterocycles. To optimize synthetic efficiency, process economics and product quality, the development of one-pot systems catalyzed by a robust catalyst featuring multi-functionality and high atom utilization is undoubtedly the most promising choice.

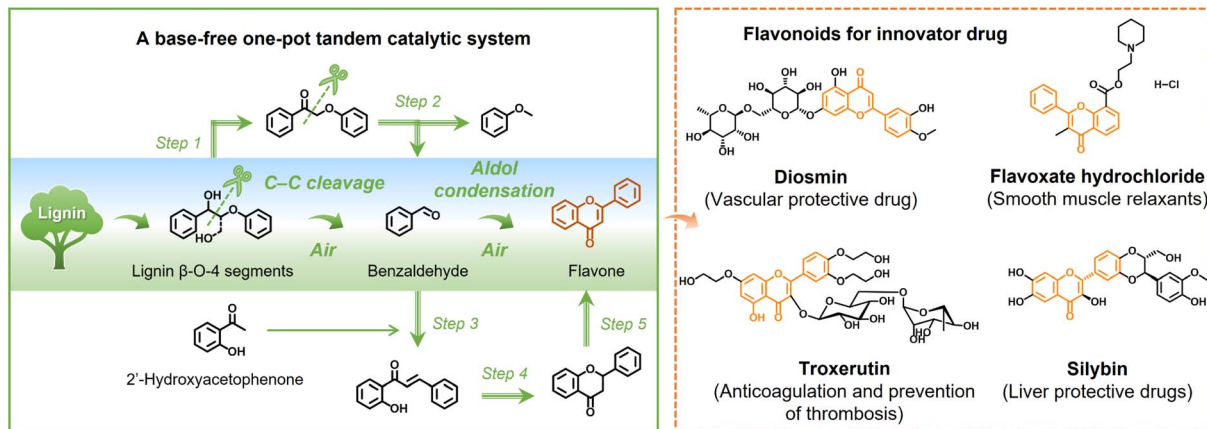
In this work, we present a three-dimensional (3D) superstructure catalyst featuring subnanometric Fe–O clusters anchored on atomically dispersed Ni-doped  $\text{ZrO}_2$  mesoporous

<sup>a</sup>State Key Laboratory of Pulp and Paper Engineering, Guangdong Provincial Key Laboratory of Fuel Cell Technology, School of Chemistry and Chemical Engineering, South China University of Technology, Guangzhou 510640, China. E-mail: [fangrq@scut.edu.cn](mailto:fangrq@scut.edu.cn); [liyw@scut.edu.cn](mailto:liyw@scut.edu.cn)

<sup>b</sup>CAS Key Laboratory of Science and Technology on Applied Catalysis, Dalian Institute of Chemical Physics, Chinese Academy of Sciences, Dalian 116023, China

<sup>c</sup>University of Chinese Academy of Sciences, Beijing 100049, China

† Electronic supplementary information (ESI) available. See DOI: <https://doi.org/10.1039/d5sc02215k>



**Scheme 1** Schematic illustration of the one-pot tandem reaction for upgrading lignin  $\beta$ -O-4 segments into flavones and the application of flavonoids.

nanosheets (denoted as  $\text{Fe}_3@\text{Ni}_1\text{-ZrO}_2$ ). This precisely engineered configuration achieves one-pot multistep conversion of lignin  $\beta$ -O-4 segments into flavones under an air atmosphere without requiring acidic or alkaline additives. Mechanistic investigations combining controlled experiments with density functional theory (DFT) calculations reveal the unique compositional features and structural advantages of  $\text{Fe}_3@\text{Ni}_1\text{-ZrO}_2$ . As illustrated in Scheme 1, the reaction initiates with  $\text{ZrO}_2$  nanosheets mediating selective C-C bond oxidative cleavage in  $\beta$ -O-4 segments (e.g., 2-phenoxy-1-phenylethanol), generating the benzaldehyde intermediate. Subsequently, the subnanometric  $\text{Fe}_3$  clusters activate aldol condensation between the cleavage intermediate and 2'-hydroxyacetophenone to form unsaturated carbonyl intermediates, while atomic Ni sites suppress competing pathways to govern the selectivity. Finally, a concerted cyclization-dehydrogenation process affords the synthesis of flavone.  $\text{Fe}_3@\text{Ni}_1\text{-ZrO}_2$  achieves 56.2% flavone yield with approximately 100% C-C bond cleavage selectivity while demonstrating broad substrate compatibility across diverse  $\beta$ -O-4 dimers and substituted 2'-phenoxyacetophenones, producing various flavonoids in 43.3–60.2% yields.

## Results and discussion

### Synthesis and characterization of $\text{Fe}_3@\text{Ni}_1\text{-ZrO}_2$

Fig. 1a schematically illustrates the synthesis routes of  $\text{Fe}_3@\text{Ni}_1\text{-ZrO}_2$ . PCN-222(Fe/Ni) was first synthesized *via* a solvothermal method. The X-ray diffraction (XRD) patterns of the as-synthesized PCN-222(Fe/Ni), PCN-222(Fe), PCN-222(Ni), and pristine PCN-222 exhibit high crystallinity, in good accordance with the literature (Fig. S1†).<sup>34</sup> Field-emission scanning electron microscopy (FESEM) and transmission electron microscopy (TEM) images reveal that the PCN-222(Fe/Ni) crystals possess a uniform spindle morphology with a size of *ca.* 1  $\mu\text{m}$ , a solid structure, and smooth external surfaces (Fig. S2†). Then, PCN-222(Fe/Ni) was pyrolyzed at 600  $^\circ\text{C}$  (based on thermogravimetric analysis (TGA) results, Fig. S3†) to synthesize  $\text{Fe}_3@\text{Ni}_1\text{-ZrO}_2$ .

SEM (Fig. S4a†) and TEM (Fig. 1b and c) images of  $\text{Fe}_3@\text{Ni}_1\text{-ZrO}_2$  reveal a well-preserved spindle morphology with uniform size but rough surfaces, attributed to the penetration of random nanosheets into both the interior and surface. The aberration-corrected high-angle annular dark-field scanning TEM (HAADF-STEM) image (Fig. S4b†) and the corresponding energy-dispersive X-ray spectroscopy (EDS) elemental mappings demonstrate the homogeneous distribution of Zr, O, Fe, and Ni elements

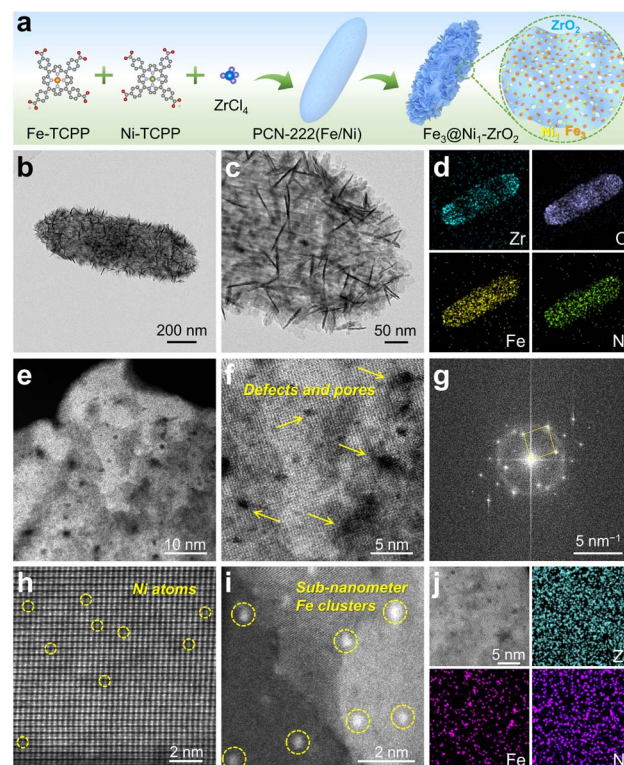


**Fig. 1** (a) Schematic illustration of the synthesis route of  $\text{Fe}_3@\text{Ni}_1\text{-ZrO}_2$ . (b and c) TEM, (d) corresponding element mapping, (e and f) HAADF-STEM, (g) SAED pattern, (h and i) AC HAADF-STEM, and (j) element mapping in high-resolution scale images of  $\text{Fe}_3@\text{Ni}_1\text{-ZrO}_2$ .

throughout the architecture, with no obvious agglomeration (Fig. 1d). This observation is further supported by elemental line-scan profiles (Fig. S4c and d†). HAADF-STEM images of localized regions (Fig. 1e and f) unambiguously uncover the mesoporous structure of the  $\text{ZrO}_2$  nanosheets. Additionally,  $\text{N}_2$  adsorption–desorption isotherms (Fig. S5†) of  $\text{Fe}_3@\text{Ni}_1\text{-ZrO}_2$  exhibit a specific surface area of  $377.8 \text{ m}^2 \text{ g}^{-1}$ , while pore size distribution curves indicate the presence of mesopores ranging predominantly from 2 to 40 nm. The selected-area electron diffraction (SAED) patterns (Fig. 1g) display distinct spotty diffraction rings, indicating the single-crystalline nature of the  $\text{ZrO}_2$  nanosheets. The spherically aberration-corrected HAADF-STEM (AC HAADF-STEM) image (Fig. 1h) resolves atomically dispersed Ni atoms (isolated dark dots) within the  $\text{ZrO}_2$  lattice

and sub-nanometer Fe clusters (Fig. 1i). Moreover, high-resolution elemental mappings (Fig. 1j) corroborate the atomic dispersion of Ni species and the localized Fe clusters. Finally, characterization of the counterparts ( $\text{Fe}_3@\text{ZrO}_2$ ,  $\text{Ni}_1\text{-ZrO}_2$ , and  $\text{ZrO}_2$ ) confirms their analogous structural features (Fig. S6–S8†).

The XRD patterns of  $\text{Fe}_3@\text{Ni}_1\text{-ZrO}_2$  (Fig. 2a) exhibit only weak crystalline phases of monoclinic  $\text{ZrO}_2$  (m- $\text{ZrO}_2$ ), which can be attributed to its two-dimensional (2D) sheet-like morphology. Furthermore, no characteristic peaks corresponding to metallic Fe or Ni are detected, possibly due to their atomic-scale dispersion. Inductively coupled plasma optical emission spectrometer (ICP-OES) analysis (Table S1†) reveals that the Zr, Fe, and Ni contents in  $\text{Fe}_3@\text{Ni}_1\text{-ZrO}_2$  are 26.8, 4.4, and 0.8 wt%, respectively. In addition, the XRD patterns

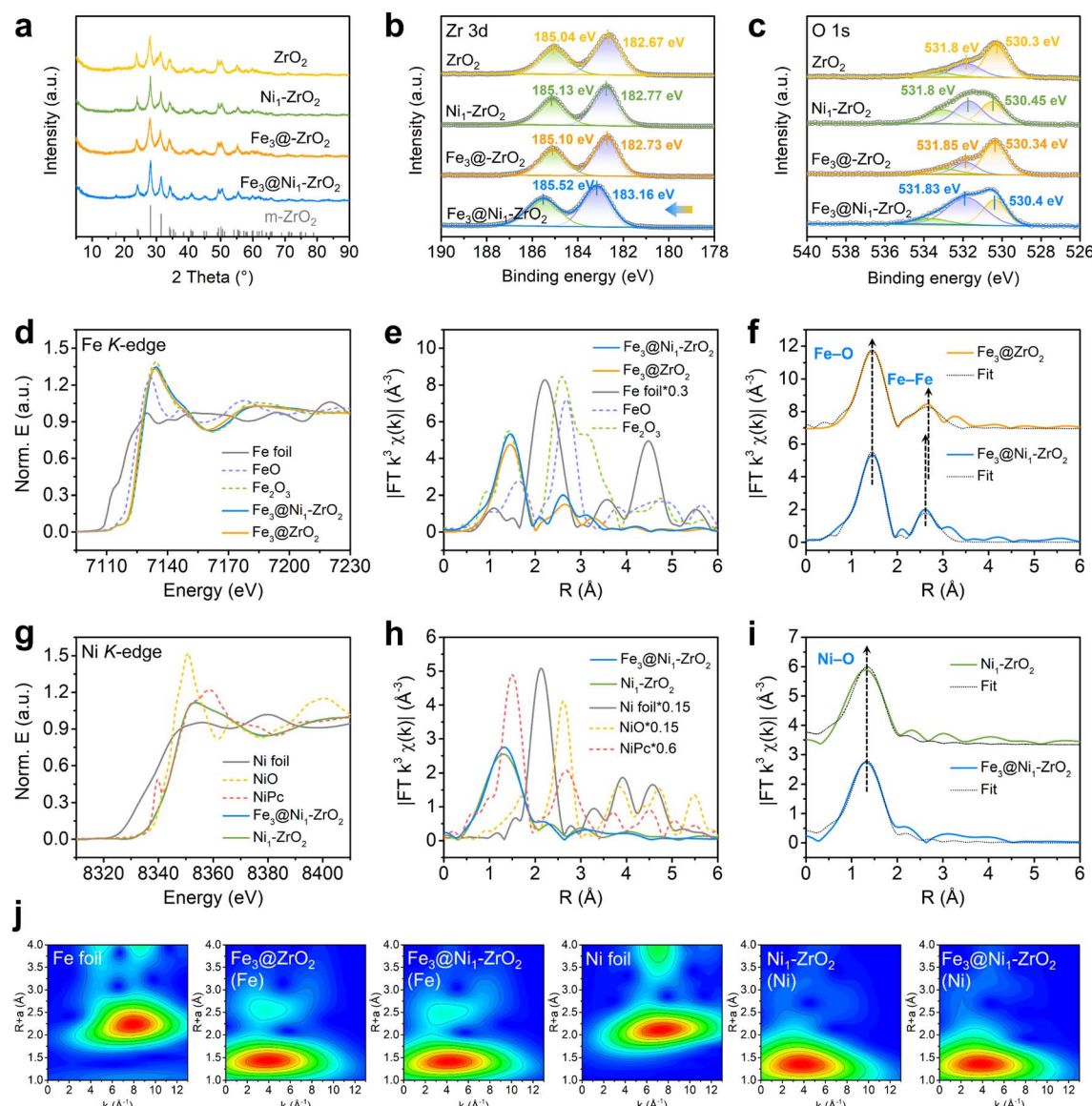


Fig. 2 (a) XRD patterns and XPS spectra in (b) the Zr 3d region and (c) the O 1s region of  $\text{Fe}_3@\text{Ni}_1\text{-ZrO}_2$ ,  $\text{Fe}_3@\text{ZrO}_2$ ,  $\text{Ni}_1\text{-ZrO}_2$ , and  $\text{ZrO}_2$ . (d) XANES spectra at the Fe K-edge, (e) Fourier transform (FT) at the Fe K-edge, (f) corresponding EXAFS fitting curves of  $\text{Fe}_3@\text{ZrO}_2$  (Fe) and  $\text{Fe}_3@\text{Ni}_1\text{-ZrO}_2$  (Fe) in R-space, (g) XANES spectra at the Ni K-edge, (h) Fourier transform (FT) at the Ni K-edge, (i) corresponding EXAFS fitting curves of  $\text{Ni}_1\text{-ZrO}_2$  (Ni) and  $\text{Fe}_3@\text{Ni}_1\text{-ZrO}_2$  (Ni) in R-space, and (j) WT  $k^3$ -weighted EXAFS spectra.



(Fig. 2a) do not show clear characteristic peaks of carbon due to its amorphous nature in  $\text{Fe}_3@\text{Ni}_1\text{-ZrO}_2$ . X-ray photoelectron spectroscopy (XPS) analysis of C 1s (Fig. S9†) indicates that carbon species predominantly exist as C–C and C=O bonds, accompanied by a small amount of O–C=O groups. In the Zr 3d region (Fig. 2b), the characteristic doublet peaks of Zr<sup>4+</sup> are observed at binding energies of 183.16 and 185.52 eV. Notably, the Zr<sup>4+</sup> peaks in  $\text{Fe}_3@\text{Ni}_1\text{-ZrO}_2$  exhibit a distinct shift toward higher binding energy (*ca.* 0.49 eV), suggesting electron transfer from Zr to Fe or Ni atoms. A similar shift is observed for Zr<sup>4+</sup> in both  $\text{Fe}_3@\text{ZrO}_2$  and  $\text{Ni}_1\text{-ZrO}_2$ , with the latter showing a more pronounced shift, possibly due to the doping effect of Ni atoms in the  $\text{ZrO}_2$  lattice. The high-resolution O 1s XPS spectrum (Fig. 2c) is deconvoluted into three components at 530.4, 531.83, and 533.0 eV, corresponding to lattice oxygen (metal–O bonds), oxygen vacancies, and surface-adsorbed oxygen species, respectively.<sup>35–37</sup>

The chemical states and coordination environments of atomic Fe and Ni species in  $\text{Fe}_3@\text{Ni}_1\text{-ZrO}_2$  and the counterparts ( $\text{Fe}_3@\text{ZrO}_2$  and  $\text{Ni}_1\text{-ZrO}_2$ ) were further investigated using XPS and X-ray absorption fine spectroscopy (XAFS, Fig. 2d–j, S10–S15, and Tables S2 and S3†).<sup>38</sup> The Fe K-edge X-ray absorption near-edge structure (XANES) spectra (Fig. 2d, S10a, b and S11a–c†) show that the absorption threshold position is located between  $\text{FeO}$  and  $\text{Fe}_2\text{O}_3$ , indicating an intermediate oxidation state of Fe between +2 and +3 in both  $\text{Fe}_3@\text{Ni}_1\text{-ZrO}_2$  and  $\text{Fe}_3@\text{ZrO}_2$ . This observation is corroborated by high-resolution Fe 2p XPS spectra (Fig. S12a†), and the Fe 2p<sub>3/2</sub> peak at 711.04 eV corresponds to positively charged Fe species (close to Fe<sup>2+</sup>). Fourier transformed (FT) Fe K-edge extended X-ray absorption fine structure (EXAFS) analysis of  $k^3$ -weighted spectra in R-space (Fig. 2e) reveals a dominant peak centered at 1.46 Å, assigned to the first-shell Fe–O coordination. This suggests that the local Fe coordination in  $\text{Fe}_3@\text{Ni}_1\text{-ZrO}_2$  and  $\text{Fe}_3@\text{ZrO}_2$  is similar to that of the  $\text{Fe}_2\text{O}_3$  reference. A minor second-shell Fe–Fe correlation peak is observed at 2.61 Å for  $\text{Fe}_3@\text{Ni}_1\text{-ZrO}_2$  and 2.66 Å for  $\text{Fe}_3@\text{ZrO}_2$ , with the shorter distance in the former likely attributable to enhanced electron transfer between  $\text{Fe}_3$  and  $\text{Ni}_1\text{-ZrO}_2$  after Ni doping. Quantitative fitting (Fig. 2f and Table S2†) further confirms that  $\text{Fe}_3@\text{Ni}_1\text{-ZrO}_2$  exhibits an Fe–Fe coordination number of *ca.* 3 (lower than the  $\text{Fe}_2\text{O}_3$  reference), an average Fe–Fe bond length of 3.08 Å (much shorter than the  $\text{Fe}_2\text{O}_3$  reference), and an average Fe–O bond length of 1.98 Å (comparable to the  $\text{Fe}_2\text{O}_3$  reference).<sup>39</sup> These findings are consistent with wavelet transform (WT) analysis (Fig. 2j and S13a†), which identifies Fe–O and Fe–Fe bonding features, consistent with the EXAFS results.

The Ni K-edge XANES spectra of  $\text{Fe}_3@\text{Ni}_1\text{-ZrO}_2$  and  $\text{Ni}_1\text{-ZrO}_2$  (Fig. 2g, S10c, d and S11d–f†) disclose a +2 oxidation state for Ni. The high-resolution Ni 2p XPS spectra (Fig. S12b†) show that the Ni 2p<sub>3/2</sub> peaks of both  $\text{Fe}_3@\text{Ni}_1\text{-ZrO}_2$  and  $\text{Ni}_1\text{-ZrO}_2$  are located at 855.11 eV, which is assigned to Ni<sup>2+</sup>. In the Ni K-edge FT-EXAFS spectra (Fig. 2h), one dominant peak at 1.31 Å (phase-uncorrected) is observed in both  $\text{Fe}_3@\text{Ni}_1\text{-ZrO}_2$  and  $\text{Ni}_1\text{-ZrO}_2$ , attributed to the Ni–O coordination shell. The quantitative least-squares EXAFS curve-fitting analysis (Fig. 2i) reveals a phase-corrected Ni–O bond length of 1.92 Å in both  $\text{Fe}_3@\text{Ni}_1\text{-ZrO}_2$  and  $\text{Ni}_1\text{-ZrO}_2$ , which is shorter than that of the  $\text{NiO}$  reference (2.09 Å), indicative of lattice distortion due to Ni<sup>2+</sup> doping into  $\text{ZrO}_2$ . Moreover, the absence of peaks near *ca.* 2.13 Å (metallic Ni–Ni in Ni foil) or 2.95 Å ( $\text{NiO}$  reference second shell) confirms the atomic dispersion of Ni species in  $\text{Fe}_3@\text{Ni}_1\text{-ZrO}_2$  and  $\text{Ni}_1\text{-ZrO}_2$ . Furthermore, the WT of Ni K-edge EXAFS oscillations (Fig. 2j and S13b†) displays a prominent intensity maximum at approximately 3.9 Å<sup>–1</sup>, corresponding to the Ni–O coordination environment, which further excludes metallic Ni contributions.

Based on these results, optimized structural models of  $\text{Fe}_3@\text{Ni}_1\text{-ZrO}_2$  and related counterparts (*i.e.*,  $\text{Fe}_3@\text{ZrO}_2$ ,  $\text{Ni}_1\text{-ZrO}_2$ , and  $\text{ZrO}_2$ ) were constructed (Fig. S14†). Charge density difference plots reveal distinct electronic redistributions, *i.e.*, in pristine  $\text{ZrO}_2$  (Fig. S15d†), electron accumulation around O atoms and depletion around Zr atoms. After Ni-doping to obtain  $\text{Ni}_1\text{-ZrO}_2$ , the charge density around O atoms reduces slightly, while mild electron depletion occurs around Ni atoms (Fig. S15c†). Bader charge analysis indicates that each Ni atom carries an average charge of +0.361|e|, whereas the charges on Zr (+2.52|e| *vs.* 2.42|e| in pristine  $\text{ZrO}_2$ ) and O (–1.36|e| *vs.* –1.38|e| in pristine  $\text{ZrO}_2$ ) atoms increase, confirming electron transfer from Ni to  $\text{ZrO}_2$ . For  $\text{Fe}_3@\text{Ni}_1\text{-ZrO}_2$  (Fig. S15a†), the average charge on each Ni atom decreases significantly to +0.027|e| (compared to +0.361|e| in  $\text{Ni}_1\text{-ZrO}_2$ ), while each Fe atom carries an average charge of +0.262|e|. Specifically, individual Fe atoms exhibit charges of +0.556|e| (1-Fe), –0.112|e| (2-Fe), and +0.333|e| (3-Fe), respectively. In contrast, Fe atoms in  $\text{Fe}_3@\text{ZrO}_2$  (Fig. S15b†) carry charges of –0.29|e| (1-Fe), –0.877|e| (2-Fe), and –0.492|e| (3-Fe), respectively, with an average of –0.553|e|. These results suggest charge transfer from the  $\text{Fe}_3$  cluster to the Ni atom in  $\text{Fe}_3@\text{Ni}_1\text{-ZrO}_2$ . Furthermore, the projected density-of-states (pDOS) demonstrates enhanced electronic states near the Fermi level for all models, particularly in  $\text{Fe}_3@\text{Ni}_1\text{-ZrO}_2$  (Fig. S16†).

### Catalytic performance of $\text{Fe}_3@\text{Ni}_1\text{-ZrO}_2$

Next, the as-prepared  $\text{Fe}_3@\text{Ni}_1\text{-ZrO}_2$  was subsequently employed for upgrading lignin β-O-4 segments into flavonoid natural products. A one-pot cascade conversion of 2-phenoxy-1-phenylethanol (**1a**) and 2'-hydroxyacetophenone (**1b**) to flavone (**6a**) was investigated as a model reaction (Fig. 3a). The proposed mechanism involves four key steps. Specifically, **1a** first undergoes oxidation to 2'-phenoxyacetophenone (**2a**) and subsequent C–C bond cleavage to generate the key intermediate, *i.e.*, benzaldehyde (**3a**). Another product is anisole that consistently exists in the catalytic system and is not involved in any subsequent reactions, whose yield is shown in Table S4.† Next, **3a** reacts with **1b** to obtain 2'-hydroxychalcone (**4a**) through a C–C coupling reaction, which then undergoes intramolecular self-cyclization to form a flavanone (**5a**). Finally, **5a** evolves into the target product flavone (**6a**) through oxidative dehydrogenation.

Under optimized conditions (150 °C, 0.5 MPa air, and 30 h),  $\text{Fe}_3@\text{Ni}_1\text{-ZrO}_2$  affords 56.2% yield of flavone (**6a**) at 78.1% conversion of **1a** (Fig. 3b and Table S4†), with a turnover



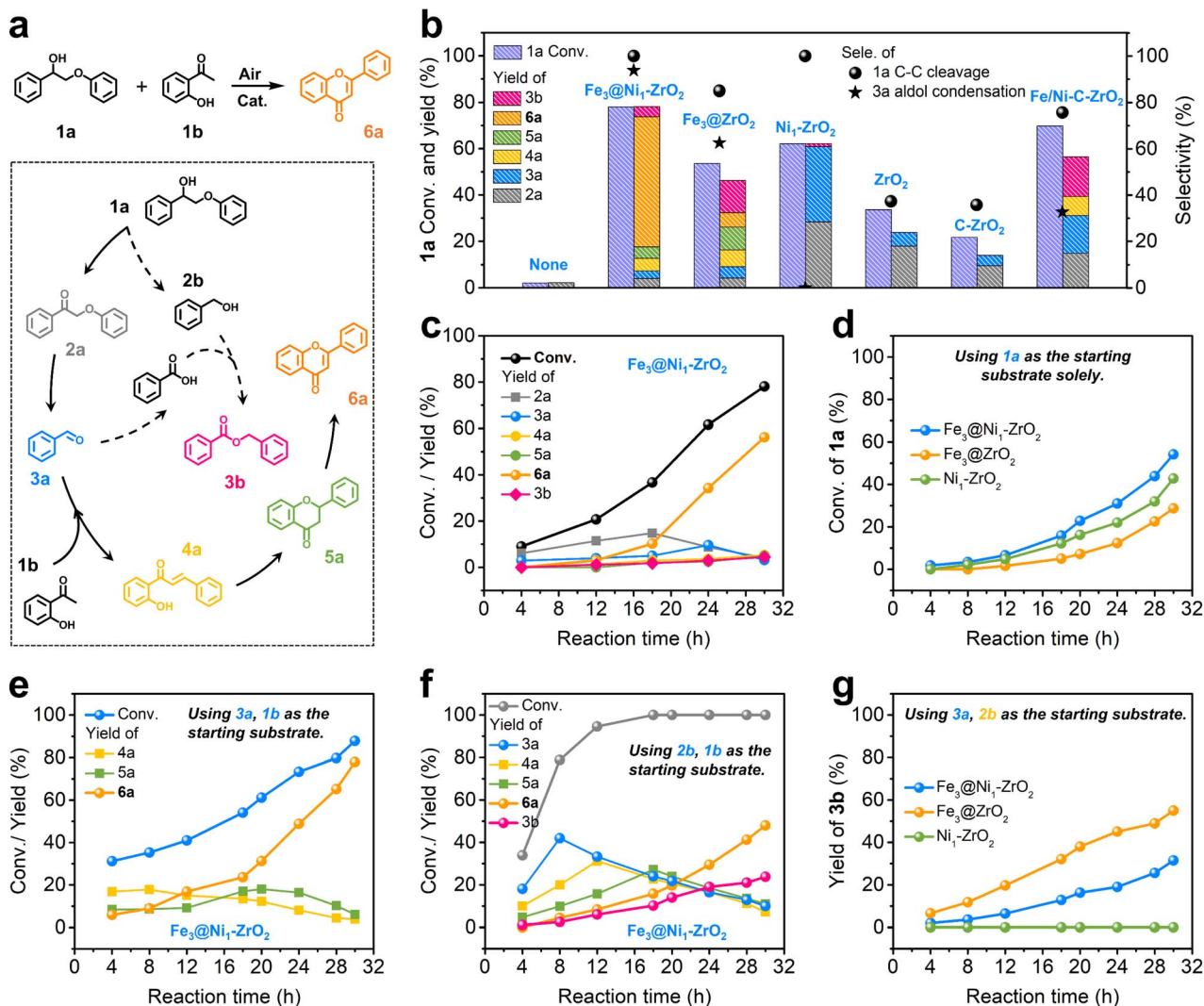


**Fig. 3** (a) Possible reaction route. (b) Catalytic performance of different catalysts. Reaction conditions: 2-phenoxy-1-phenylethanol (1a, 1 mmol), 2'-hydroxyacetophenone (1b, 1.2 mmol), catalyst (0.05 g), toluene (3 mL), 150 °C, 30 h, and air (0.5 MPa). (c) Conversion and yield as a function of reaction time in the proposed one-pot cascade catalytic system over Fe<sub>3</sub>@Ni<sub>1</sub>-ZrO<sub>2</sub>. Reaction conditions: 2-phenoxy-1-phenylethanol (1a, 1 mmol), 2'-hydroxyacetophenone (1b, 1.2 mmol), catalyst (0.05 g), toluene (3 mL), 150 °C, and air (0.5 MPa). (d) Control experiments using 2-phenoxy-1-phenylethanol (1a) as the only substrate. Reaction conditions: 2-phenoxy-1-phenylethanol (1a, 1 mmol), catalyst (0.05 g), toluene (3 mL), 150 °C, 30 h, and air (0.5 MPa). (e) Control experiments using 3a and 1b as the substrates over Fe<sub>3</sub>@Ni<sub>1</sub>-ZrO<sub>2</sub>. (f) Control experiments using 2b and 1b as the substrates over Fe<sub>3</sub>@Ni<sub>1</sub>-ZrO<sub>2</sub>. (g) Control experiments using 3a and 2b as the substrates.

number (TON) of 4.04 (Table S4†). The time-tracking experiment (Fig. 3c and Table S5†) revealed sequential formation and consumption of intermediates 2a (maximum yield at 18 h) and 3a (maximum yield at 24 h), consistent with a stepwise pathway involving oxidation of 1a to 2a, followed by C–C cleavage to 3a. Notably, no C–O cleavage by-products were detected. Control experiments (Fig. 3b and Table S4†) confirmed the necessity of both the catalyst and air (as the terminal oxidant), with reactive oxygen species (ROS) identified as superoxide radicals (·O<sub>2</sub><sup>−</sup>) via electron paramagnetic resonance (EPR) analysis (Fig. S17†).

To benchmark the performance of Fe<sub>3</sub>@Ni<sub>1</sub>-ZrO<sub>2</sub>, control experiments were conducted with its counterparts (Fe<sub>3</sub>@ZrO<sub>2</sub>, Ni<sub>1</sub>-ZrO<sub>2</sub>, and ZrO<sub>2</sub>) under identical reaction conditions (Fig. 3b and Table S4†). Fe<sub>3</sub>@ZrO<sub>2</sub> achieved 53.6% conversion of 2-

phenoxy-1-phenylethanol (1a) with 85.0% selectivity toward C–C bond cleavage, yielding only 6.3% flavone (6a) alongside 13.9% benzyl benzoate (3b). The latter by-product is probably formed via esterification of 2b with benzoic acid, generated through oxidation of intermediate 3a (dashed pathway in Fig. 3a). Ni<sub>1</sub>-ZrO<sub>2</sub> and ZrO<sub>2</sub> afforded 62.1% and 33.6% conversion of 2-phenoxy-1-phenylethanol (1a), respectively, but failed to produce flavone (6a). Notably, Ni<sub>1</sub>-ZrO<sub>2</sub> exhibited 100% selectivity toward C–C bond cleavage, whereas ZrO<sub>2</sub> showed 37.3% selectivity. These results highlight the critical role of both sub-nanometric Fe<sub>3</sub> clusters and atomically dispersed Ni species in enhancing the catalytic activity of ZrO<sub>2</sub> (validated via control experiments and DFT calculations; Fig. 3d and 4). Specifically, sub-nanometric Fe<sub>3</sub> clusters uniquely drive flavone synthesis,

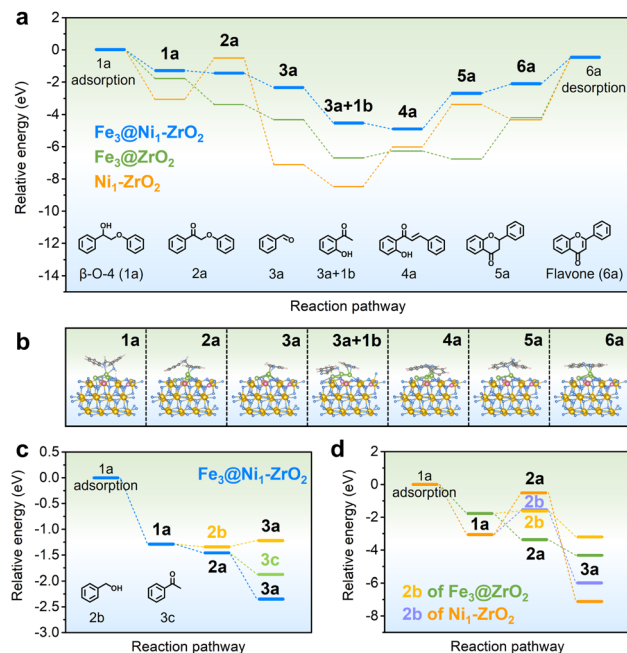


Fig. 4 (a–c) Free energy diagram of the one-pot oxidative tandem reaction for synthesis of flavone from 2-phenoxy-1-phenylethanol (**1a**), and (d) the simplified surface structures of various reaction species along the reaction pathway over  $\text{Fe}_3@\text{Ni}_1\text{-ZrO}_2$ . Fe (green), Ni (pink), Zr (yellow), O (blue), C (gray), and H (pink white).

while atomic Ni sites optimize selectivity by suppressing side reactions (further supported by control experiments and DFT calculations; Fig. 3d and 4). In addition, commercially available bulk  $\text{ZrO}_2$  and impregnation-calcination-derived  $\text{Ni}/\text{Fe-ZrO}_2$  (see the ESI† for synthesis details) were tested but showed negligible activity (Fig. 3b), underscoring the superiority of the elaborately engineered  $\text{Fe}_3@\text{Ni}_1\text{-ZrO}_2$ .

To further probe the reaction mechanism, the oxidative cleavage of 2-phenoxy-1-phenylethanol (**1a**) was independently investigated (Fig. 3d and S18†). The results show that **1a** conversion (54.2%) in this isolated cleavage system was notably lower than that in the one-pot tandem system (78.1%) under identical reaction conditions, demonstrating that the tandem process enhances oxidative cleavage efficiency by continuously removing intermediates (e.g., benzaldehyde (**3a**) and benzoic acid) through downstream reactions. These intermediates also rationalize the formation of esterification by-products (e.g., benzyl benzoate) observed in the one-pot system. Additionally, the results once again confirm that the dual-active-site catalyst  $\text{Fe}_3@\text{Ni}_1\text{-ZrO}_2$  (containing atomically dispersed Fe and Ni species) exhibits superior activity compared to single-active-site analogues ( $\text{Fe}_3@\text{ZrO}_2$  and  $\text{Ni}_1\text{-ZrO}_2$ ).

Next, reactions using 2'-hydroxyacetophenone (**1b**) and benzaldehyde (**3a**) or benzyl alcohol (**2b**) as substrates were systematically investigated (Fig. 3e and f). The synthesis of flavone (**6a**) proceeds predominantly *via* aldol condensation between intermediates **1b** and **3a**, rather than between **1b** and **2b**. The formation of benzyl benzoate (**3b**) as a by-product in the reaction of **1b** and **2b** suggests competing esterification

alongside the aldol condensation pathway in systems containing **2b** (Fig. 3f). Mechanistic investigation of the reaction between **3a** and **2b** (Fig. 3g) uncovered critical catalyst specificity, *i.e.*,  $\text{Ni}_1\text{-ZrO}_2$  exhibited negligible oxidative esterification activity, aligning with the absence of both flavone (**6a**) and benzyl benzoate (**3b**) production in the one-pot tandem system (Fig. 3b). In contrast,  $\text{Fe}_3@\text{ZrO}_2$  afforded 55.0% yield of **3b**, while  $\text{Fe}_3@\text{Ni}_1\text{-ZrO}_2$  only gives 31.5% **3b** yield, demonstrating that atomic Ni-doping could suppress oxidative esterification partly, thereby optimizing one-pot tandem reaction selectivity. Control experiments confirmed the reaction pathway, *i.e.*, **1a** is first oxidized to **2a**, which undergoes C–C cleavage to generate **3a**. Subsequently, **3a** reacts with **1b** to form **4a**, followed by cyclization to **5a** and final oxidative dehydrogenation to **6a**. Parallelly, **2b** (derived from C–C cleavage of **1a**) reacts with benzenic acid (oxidative product of **3a**) to form by-product **3b**.

The proposed one-pot catalytic system for flavone synthesis represents the first integration of 2-phenoxy-1-phenylethanol (**1a**) and aldehyde-ketone coupling within a single catalytic system, demonstrating a novel route to directly obtaining natural products from lignin  $\beta$ -O-4 segments. Notably, this process operates under base-free conditions, a significant advantage over most state-of-the-art systems for flavone synthesis or lignin  $\beta$ -O-4 segment cleavage, which require strong bases as essential additives.<sup>25–27,40</sup> We speculate that the absence of additional alkaline additives in this one-pot transformation system is due to the inherent acidity of the  $\text{ZrO}_2$  component in  $\text{Fe}_3@\text{Ni}_1\text{-ZrO}_2$ , which likely facilitates proton transfer during catalysis. To probe the acidic properties of  $\text{Fe}_3@\text{Ni}_1\text{-ZrO}_2$ , pyridine-adsorbed Fourier-transform infrared spectroscopy (Py-FTIR) was employed. Characteristic peaks at 1445, 1490, 1540, and 1595  $\text{cm}^{-1}$  clearly confirm the co-existence of Lewis and Brønsted acid sites (Fig. S19†).<sup>41,42</sup> Additionally, some of the reported catalytic systems for the cleavage of lignin model compounds and for flavone synthesis are summarized in Tables S6 and S7.†

### Reaction mechanism investigations

Subsequently, density functional theory (DFT) calculations were performed to provide theoretical insights into the reaction mechanism. The proposed reaction pathway was first supported by control experiments (Fig. 4a–d). In the adsorption configurations, **1a** was adsorbed onto  $\text{Fe}_3@\text{Ni}_1\text{-ZrO}_2$  through two O atoms, one from the C–O bond and the other from the –OH group bonded to an Fe atom, with an adsorption energy of  $-1.29$  eV. A structurally analogous adsorption mode was observed on  $\text{Fe}_3@\text{ZrO}_2$  (Fig. 4a, b and S20†). In contrast, adsorption of **1a** onto  $\text{Ni}_1\text{-ZrO}_2$  *via* a single O atom of the –OH group bonded to a Zr atom (Fig. 4a and S21†). Two possible evolutionary intermediates (**2a** or **2b**) were identified following **1a** adsorption. On both  $\text{Fe}_3@\text{Ni}_1\text{-ZrO}_2$  and  $\text{Fe}_3@\text{ZrO}_2$ , the exothermic oxidation of **1a** to **2a** is thermodynamically favoured, with energy changes of  $-0.16$  eV (*vs.*  $-0.05$  eV for **2b**) and  $-1.6$  eV (*vs.*  $0.17$  eV for **2b**), respectively. However, the conversion of **1a** to **2b** is more favorable than to **2a** on  $\text{Ni}_1\text{-ZrO}_2$ , as evidenced by the lower energy barrier ( $1.48$  eV for **2b** *vs.*  $2.55$  eV



for **2a**) (Fig. 4a–d and S20–S22†). These findings highlight that  $\text{Fe}_3$  clusters enhance catalytic activity through two synergistic effects, *i.e.*, strengthened substrate adsorption during the **1a** to **2a** (or **2b**) step and preferential generation of the **2a** intermediate over catalysts containing  $\text{Fe}_3$  clusters.

Subsequently, the C–C bond cleavage of intermediate **2a** generates the **3a** intermediate, a thermodynamically favorable process with reaction energies of  $-0.89$  eV and  $-0.95$  eV on  $\text{Fe}_3@\text{Ni}_1\text{-ZrO}_2$  and  $\text{Fe}_3@\text{ZrO}_2$ , respectively. To assess competing pathways, we examined the alternative C–O bond cleavage route leading to acetophenone (**3c**). Comparative analysis revealed strong preference for C–C cleavage over C–O bond scission, as evidenced by the significantly lower reaction energies for the former pathway ( $-0.89$  eV *vs.*  $-0.43$  eV on  $\text{Fe}_3@\text{Ni}_1\text{-ZrO}_2$ ;  $-0.95$  eV *vs.*  $0.17$  eV on  $\text{Fe}_3@\text{ZrO}_2$ ) (Fig. 4a, c, d, S20 and S22†). Notably,  $\text{Ni}_1\text{-ZrO}_2$  exhibited distinct behavior; oxidation of intermediate **2b** to **3a** proceeded with an exceptionally large thermodynamic driving force ( $-4.4$  eV; Fig. 4a, d and S21†). In addition, the potential oxidation of **2b** to **3a** on  $\text{Fe}_3@\text{Ni}_1\text{-ZrO}_2$  and  $\text{Fe}_3@\text{ZrO}_2$  requires an energy barrier of  $0.12$  eV and  $-1.59$  eV. Collectively, these computational results demonstrate that **3a** intermediate formation is energetically feasible across all catalytic systems, which aligns with experimental observations, where **3a** and its derivatives were consistently detected in all three catalytic systems.

DFT calculations further delineate distinct mechanistic pathways across catalytic systems. The oxidation of **1a** to **2a** emerges as the predominant pathway, though **2b** forms as a minor by-product through alternative routes (Fig. 4a–d). Control experiments corroborate this mechanistic dichotomy; oxidative esterification between **3a** and **2b** generates by-product **3b** in both  $\text{Fe}_3$ -containing systems ( $\text{Fe}_3@\text{Ni}_1\text{-ZrO}_2$  and  $\text{Fe}_3@\text{ZrO}_2$ ), as evidenced in Fig. 3b and g. Notably,  $\text{Ni}_1\text{-ZrO}_2$  exhibits different behavior; the formation of **2a** is thermodynamically unfavorable, requiring a high reaction energy of  $2.55$  eV (Fig. 4a–d). In contrast, **2b** emerges as the dominant product on  $\text{Ni}_1\text{-ZrO}_2$  with a significantly lower energy barrier of  $1.48$  eV. This primary intermediate (**2b**) then undergoes spontaneous conversion to **3a** with substantial exothermicity ( $\Delta E = -4.4$  eV; Fig. 4d). These results suggest that **3a** is generated later than **2b** on  $\text{Ni}_1\text{-ZrO}_2$ , whereas the formation of **3b** as a by-product is difficult in this case, consistent with experimental data (Fig. 3b and g).

The reaction pathway proceeds *via* aldol condensation between intermediates **3a** and **1b** to form **4a**. This step is exothermic on  $\text{Fe}_3@\text{Ni}_1\text{-ZrO}_2$  ( $-0.39$  eV), but becomes progressively less favorable on  $\text{Fe}_3@\text{ZrO}_2$  ( $0.43$  eV) and  $\text{Ni}_1\text{-ZrO}_2$  ( $2.46$  eV). This computational prediction aligns closely with experimental observations (Fig. 4a, b, S20 and S21†), where efficient **4a** formation was exclusively observed in the  $\text{Fe}_3@\text{Ni}_1\text{-ZrO}_2$  system. These findings highlight the unique catalytic role of  $\text{Fe}_3$  clusters in facilitating the conversion of **3a** to **4a**. Conversely, the absence of  $\text{Fe}_3$  clusters in  $\text{Ni}_1\text{-ZrO}_2$  creates an energy barrier that effectively suppresses **4a** generation. The thermodynamically accessible **4a** in the  $\text{Fe}_3@\text{Ni}_1\text{-ZrO}_2$  system serves as a key precursor, enabling subsequent transformations for **6a**.

The subsequent transformation of **4a** to **5a** on  $\text{Fe}_3@\text{Ni}_1\text{-ZrO}_2$  requires overcoming an energy barrier of  $2.22$  eV, whereas it exhibits a reaction energy of  $-0.5$  eV on  $\text{Fe}_3@\text{ZrO}_2$ . Further conversion of **5a** to **6a** remains energetically challenging for both  $\text{Fe}_3$ -containing catalysts;  $\text{Fe}_3@\text{Ni}_1\text{-ZrO}_2$  demonstrates relatively low endothermicity ( $\Delta E = 0.55$  eV), while  $\text{Fe}_3@\text{ZrO}_2$  encounters a substantial energy barrier ( $\Delta E = +2.56$  eV; Fig. 4a). This thermodynamic contrast manifests experimentally in the pronounced accumulation of **5a** observed exclusively in  $\text{Fe}_3@\text{ZrO}_2$  systems (Fig. 3b). Notably, the final desorption of **6a** from  $\text{Fe}_3@\text{Ni}_1\text{-ZrO}_2$  requires an energy barrier of  $1.66$  eV, which likely contributes to the prolonged reaction duration in this system (Fig. 4a and b). For  $\text{Fe}_3@\text{ZrO}_2$ , the desorption of **6a** requires overcoming an energy barrier as high as  $3.74$  eV, also consistent with the experimental observation of a low **6a** product yield. For  $\text{Ni}_1\text{-ZrO}_2$ , initial **4a** generation demands a  $2.46$  eV energy change, followed by a prohibitive  $2.64$  eV barrier for transforming **4a** to **5a**. This dual kinetic impediment correlates directly with experimental observations, where the  $\text{Ni}_1\text{-ZrO}_2$  system showed negligible **6a** production (Fig. 3b).

### Reusability and stability of $\text{Fe}_3@\text{Ni}_1\text{-ZrO}_2$

The used  $\text{Fe}_3@\text{Ni}_1\text{-ZrO}_2$  catalyst was collected by centrifugation and demonstrated direct reusability for six runs without significant activity loss (Fig. S23†), confirming its good recyclability. Characterization results (Fig. S24–S27†) indicate that the recycled  $\text{Fe}_3@\text{Ni}_1\text{-ZrO}_2$  retains identical structural and compositional properties compared to the fresh one. In addition, metal leaching tests and a hot filtration experiment (Fig. S28†) confirm the robust stability of  $\text{Fe}_3@\text{Ni}_1\text{-ZrO}_2$  and the heterogeneous catalytic nature of this one-pot tandem reaction.

Considering the practicality of the developed one-pot tandem catalytic system and the large-scale synthesis demand in the biopharmaceutical field, this one-pot tandem reaction system was evaluated in a continuous flow reactor to assess industrial scalability (Fig. 5a). The  $\text{Fe}_3@\text{Ni}_1\text{-ZrO}_2$  catalyst was slurry-packed with toluene and loaded into the packed column. Upon injecting a toluene solution containing 2-phenoxy-1-phenylethanol (**1a**) and 2'-hydroxyacetophenone (**1b**), the system achieved  $84.3\%$  conversion of **1a** and  $63.3\%$  yield of flavone (**6a**) (average values). Continuous operation for  $120$  h showed no notable performance degradation, delivering a space-time yield (STY) of  $3.3 \text{ g g}_{\text{cat}}^{-1} \text{ h}^{-1}$  and a turnover frequency (TOF) of  $139 \text{ h}^{-1}$ . To the best of our knowledge, this represents the first reported one-pot synthesis of flavone from lignin  $\beta$ -O-4 segments, highlighting the system's pioneering significance. Although a unified comparison standard is difficult to establish, we still compiled a comparison table (Table S8†) summarizing various flavonoid synthesis methodologies, in which the yields, substrates, and sustainability metrics from representative enzymatic, homogeneous catalytic, and our current work were included.

### Catalytic system flexibility and product practicality

In order to further demonstrate the progressiveness of the developed one-pot tandem lignin-upgrading system, we



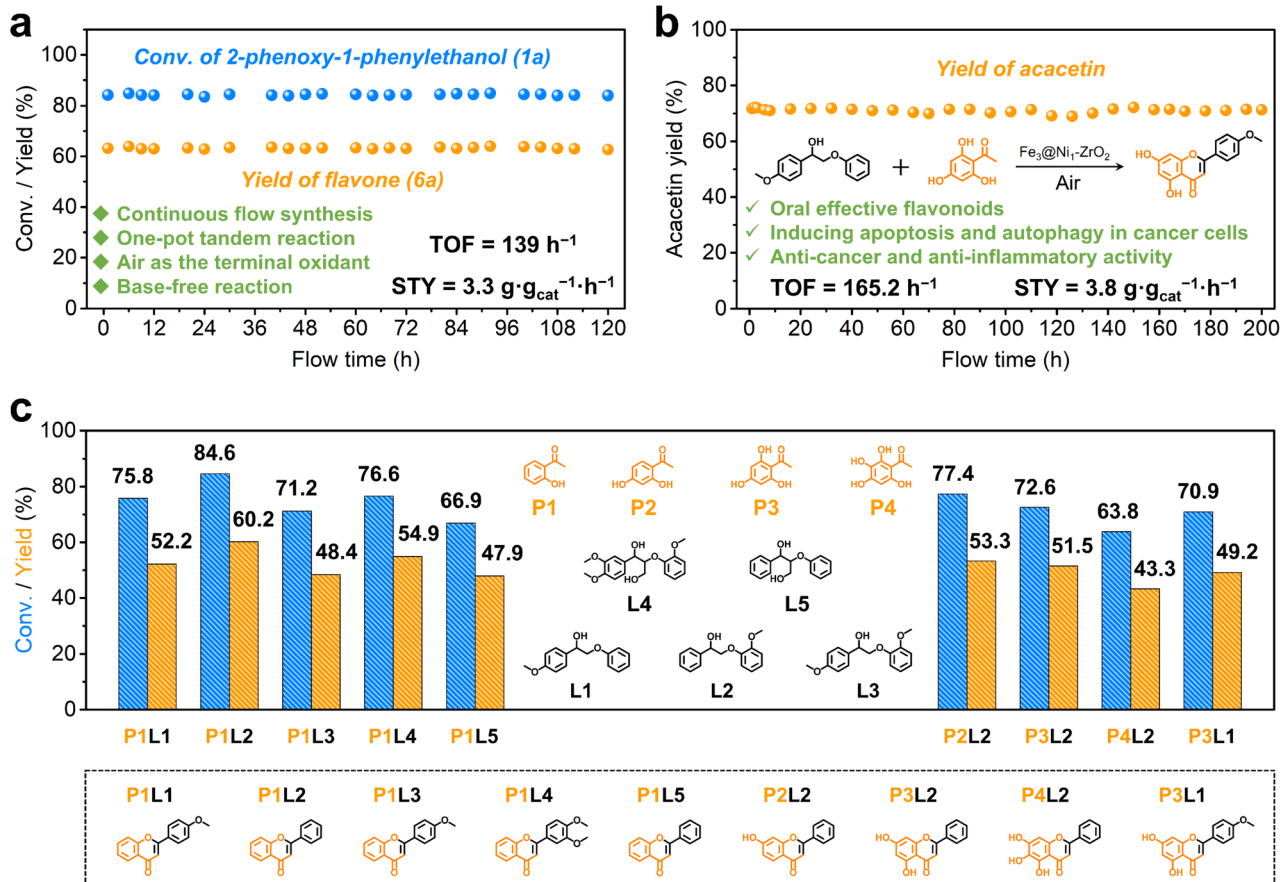


Fig. 5 (a) Catalytic system (for flavone synthesis) proceeds in a continuous flow reactor over  $\text{Fe}_3@\text{Ni}_1\text{-ZrO}_2$ . (b) The continuous flow reaction for acacetin synthesis over  $\text{Fe}_3@\text{Ni}_1\text{-ZrO}_2$ . (c) Scope of the one-pot tandem cleavage-coupling reaction for flavone synthesis over  $\text{Fe}_3@\text{Ni}_1\text{-ZrO}_2$ . Conversion and yield were determined by GC and GC-MS based on L1–L4.

evaluated the catalytic performance using additional lignin  $\beta$ -O-4 dimers (L1–L5) as substrates. Experimental results demonstrate substrate conversions of 71.2–84.6% with the corresponding flavonoid yields of 48.4–60.2% (Fig. 5c, left columns). To assess broader applicability, the system was extended to synthesize flavonoids with fantastic biological activities from substrates with different substituted groups (P1–P4), achieving yields of 43.3–53.3% (Fig. 5c, right columns).

For comprehensive assessment of the application prospective, a scale-up production of acacetin from L1 and P3 was conducted in a continuous flow reactor (Fig. 5b). The system maintained stable operation for >200 h without significant performance decay, delivering a STY up to  $3.8 \text{ g} \cdot \text{g}_{\text{cat}}^{-1} \cdot \text{h}^{-1}$  and a TOF of  $165.2 \text{ h}^{-1}$ . Acacetin was easily isolated from the crude reaction mixture by simple centrifugation and purification treatments, with structural confirmation by  $^1\text{H-NMR}$  and  $^{13}\text{C-NMR}$  spectroscopy (Fig. S29 and S30†). These results demonstrate the great application potential of this catalysis system for sustainable and large-scale flavonoid synthesis.

## Conclusions

In summary, we have developed a robust  $\text{Fe}_3@\text{Ni}_1\text{-ZrO}_2$  catalyst through atomic-level engineering of  $\text{ZrO}_2$  nanosheets with dual

metal species, which features subnanometric Fe–O clusters anchored on atomically dispersed Ni-doped  $\text{ZrO}_2$  mesoporous nanosheets. This synergistic architecture enables concerted catalysis of selective C–C bond oxidative cleavage in lignin  $\beta$ -O-4 segments and *in situ* transformation of the cleavage intermediate into flavone, establishing a highly coupled tandem process for one-pot  $\beta$ -O-4 model upgrading. Our findings propose a versatile strategy for integrating atomic-scale metal species within mesoporous metal oxide catalysts. This approach opens avenues for continuous synthesis of value-added bio-products by overcoming challenges in multistep reaction cascades, thereby advancing sustainable utilization of biomass-derived feedstocks.

## Data availability

The data supporting this article have been included as part of the ESI.†

## Author contributions

Y. L. and X. Z. developed the idea and designed experiments. X. Z. and J. W. performed the catalyst synthesis and most of the characterization studies. X. Z. and J. W. performed the electron

microscopy characterization. J. W. and R. F. performed most of the catalytic reactions. Q. Q. and D. T. synthesized substrates for the catalytic performance evaluation and performed some reaction tests. X. Z., R. F., and F. W. conducted and discussed the theoretical calculations. X. Z., C. L., R. F., and Y. L. co-wrote the manuscript. All authors discussed the results and commented on the manuscript.

## Conflicts of interest

There are no conflicts to declare.

## Acknowledgements

This work was supported by the State Key Laboratory of Pulp and Paper Engineering (2024ZD09), the National Natural Science Foundation of China (22138003, 21825802, 22408109, and 22478135), the China National Postdoctoral Program for Innovative Talents (BX20230131), the China Postdoctoral Science Foundation (2023M741209), the Natural Science Foundation of Guangdong Province (2023B1515040005), the Guangdong Basic and Applied Basic Research Foundation (2023B1515020033 and 2025A1515011981), the Young Elite Scientists Sponsorship Program by CAST (2023QNRC001), the Fundamental Research Funds for the Central Universities (2024ZYGXZR071, 2024ZYGXZR099), and the Science and Technology Program of Guangzhou City (2023A04J0673).

## References

- 1 C. Li, X. Zhao, A. Wang, G. W. Huber and T. Zhang, *Chem. Rev.*, 2015, **115**, 11559–11624.
- 2 Y. H. Liao, S.-F. Koelewijn, G. V. Bossche, J. V. Aelst, S. V. Bosch, T. Renders, K. Navare, T. Nicolaï, K. V. Aelst, M. Maesen, H. Matsushima, J. M. Thevelein, K. V. Acker, B. Lagrain, D. Verboekend and B. F. Sels, *Science*, 2020, **367**, 1385–1390.
- 3 A. Rahimi, A. Ulbrich, J. J. Coon and S. S. Stahl, *Nature*, 2014, **515**, 249–252.
- 4 G. Meng, W. Lan, L. Zhang, S. Wang, T. Zhang, S. Zhang, M. Xu, Y. Wang, J. Zhang, F. Yue, Y. Wu and D. Wang, *J. Am. Chem. Soc.*, 2023, **145**, 12884–12893.
- 5 W. Lan, M. T. Amiri, C. M. Hunston and J. S. Luterbacher, *Angew. Chem., Int. Ed.*, 2018, **57**, 1356–1360.
- 6 Y. X. Cao, G. Zhu, Y. Li, N. L. Breton, C. Gourlaouen, S. Choua, J. Boixel, H.-P. J. Rouville and J.-F. Soulé, *J. Am. Chem. Soc.*, 2022, **144**, 5902–5909.
- 7 J. Yan, Q. Meng, X. Shen, B. Chen, Y. Sun, J. Xiang, H. Liu and B. Han, *Sci. Adv.*, 2020, **6**, eabd1951.
- 8 S. S. Wong, R. Shu, J. Zhang, H. Liu and N. Yan, *Chem. Soc. Rev.*, 2020, **49**, 5510–5560.
- 9 X. Wu, N. Luo, S. Xie, H. Zhang, Q. Zhang, F. Wang and Y. Wang, *Chem. Soc. Rev.*, 2020, **49**, 6198–6223.
- 10 E. Subbotina, T. Rukkijakan, M. D. Marquez-Medina, X. Yu, M. Johnsson and J. S. M. Samec, *Nat. Chem.*, 2021, **13**, 1118–1125.
- 11 P. Sudarsanam, R. Y. Zhong, S. Van den Bosch, S. M. Coman, V. I. Parvulescu and B. F. Sels, *Chem. Soc. Rev.*, 2018, **47**, 8349–8402.
- 12 X. Wu, X. Fan, S. Xie, J. Lin, J. Cheng, Q. Zhang, L. Chen and Y. Wang, *Nat. Catal.*, 2018, **1**, 772–780.
- 13 L. Li, L. Dong, D. Li, Y. Guo, X. Liu and Y. Wang, *ACS Catal.*, 2020, **10**, 15197–15206.
- 14 Q. Wang, L.-P. Xiao, Y.-H. Lv, W.-Z. Yin, C.-J. Hou and R.-C. Sun, *ACS Catal.*, 2022, **12**, 11899–11909.
- 15 C. Zhang, H. Li, J. Lu, X. Zhang, K. E. MacArthur, M. Heggen and F. Wang, *ACS Catal.*, 2017, **7**, 3419–3429.
- 16 M. Wang, M. Liu, H. Li, Z. Zhao, X. Zhang and F. Wang, *ACS Catal.*, 2018, **8**, 6837–6843.
- 17 Q. Song, F. Wang, J. Cai, Y. Wang, J. Zhang, W. Yu and J. Xu, *Energy Environ. Sci.*, 2013, **6**, 994.
- 18 H. Li and G. Song, *ACS Catal.*, 2019, **9**, 4054–4064.
- 19 T. Cui, L. Ma, S. Wang, C. Ye, X. Liang, Z. Zhang, G. Meng, L. Zheng, H.-S. Hu, J. Zhang, H. Duan, D. Wang and Y. Li, *J. Am. Chem. Soc.*, 2021, **143**, 9429–9439.
- 20 H. Luo, E. P. Weeda, M. Alhorech, C. W. Anson, S. D. Karlen, Y. Cui, C. E. Foster and S. S. Stahl, *J. Am. Chem. Soc.*, 2021, **143**, 15462–15470.
- 21 S. Z. Wang, K. L. Zhang, H. L. Li, L. P. Xiao and G. Y. Song, *Nat. Commun.*, 2021, **12**, 416.
- 22 Z. H. Sun, G. Bottari, A. Afanasenko, M. C. A. Stuart, P. J. Deuss, B. Fridrich and K. Barta, *Nat. Catal.*, 2018, **1**, 82–92.
- 23 L. Shuai, M. T. Amiri, Y. M. Questell-Santiago, F. Héroguel, Y. Li, H. Kim, R. Meilan, C. Chapple, J. Ralph and J. S. Luterbacher, *Science*, 2016, **354**, 329–333.
- 24 H. Li, A. Bunrit, J. Lu, Z. Gao, N. Luo, H. Liu and F. Wang, *ACS Catal.*, 2019, **9**, 8843–8851.
- 25 Y. Ding, T. Guo, Z. Li, B. Zhang, F. E. Kühn, C. Liu, J. Zhang, D. Xu, M. Lei, T. Zhang and C. Li, *Angew. Chem., Int. Ed.*, 2022, **61**, e202206284.
- 26 Y. Liu, Q. Luo, Q. Qiang, H. Wang, Y. Ding, C. Wang, J. Xiao, C. Li and T. Zhang, *ChemSusChem*, 2022, **15**, e202201401.
- 27 B. Zhang, T. L. Guo, Z. W. Li, F. E. Kuhn, M. Lei, Z. B. K. Zhao, J. L. Xiao, J. Zhang, D. Z. Xu, T. Zhang and C. Z. Li, *Nat. Commun.*, 2022, **13**, 3365.
- 28 H. Xiong, H. Zhou, G. Sun, Z. Liu, L. Zhang, L. Zhang, F. Du, Z.-A. Qiao and S. Dai, *Angew. Chem., Int. Ed.*, 2020, **59**, 11053–11060.
- 29 Y. Wang, H. Arandiyani, J. Scott, A. Bagheri, H. Dai and R. Amal, *J. Mater. Chem. A*, 2017, **5**, 8825–8846.
- 30 M. Chen, Y. Zhang, L. Xing, Y. Liao, Y. Qiu, S. Yang and W. Li, *Adv. Mater.*, 2017, **29**, 1607015.
- 31 K. Liu, H. Jin, L. Huang, Y. Luo, Z. Zhu, S. Dai, X. Zhuang, Z. Wang, L. Huang and J. Zhou, *Sci. Adv.*, 2022, **8**, eabn2030.
- 32 J. Ma, Y. Ren, X. Zhou, L. Liu, Y. Zhu, X. Cheng, P. Xu, X. Li, Y. Deng and D. Zhao, *Adv. Funct. Mater.*, 2018, **28**, 1705268.
- 33 Y. Huang, S. L. Zhang, X. F. Lu, Z.-P. Wu, D. Luan and X. W. Lou, *Angew. Chem., Int. Ed.*, 2021, **60**, 11841–11846.
- 34 Q. Wang, T. Liu, K. Chen, D. Wu, C. Chen, M. Chen, X. Ma, J. Xu, T. Yao, Y. Li, H. Zhou and Y. Wu, *Small*, 2022, 2204015.
- 35 X. F. Lu, Y. Chen, S. Wang, S. Gao and X. W. Lou, *Adv. Mater.*, 2019, **31**, 1902339.



36 J. Bao, X. Zhang, B. Fan, J. Zhang, M. Zhou, W. Yang, X. Hu, H. Wang, B. Pan and Y. Xie, *Angew. Chem., Int. Ed.*, 2015, **54**, 7399–7404.

37 J. Fu, F. M. Hassan, C. Zhong, J. Lu, H. Liu, A. Yu and Z. Chen, *Adv. Mater.*, 2017, **29**, 1702526.

38 W. Lyu, Y. Liu, J. Zhou, D. Chen, X. Zhao, R. Fang, F. Wang and Y. Li, *Angew. Chem., Int. Ed.*, 2023, **62**, e202310733.

39 W. Zhao, Y. Shi, Y. Jiang, X. Zhang, C. Long, P. An, Y. Zhu, S. Shao, Z. Yan, G. Li and Z. Tang, *Angew. Chem., Int. Ed.*, 2021, **60**, 5811–5815.

40 X. Zhao, R. Fang, F. Wang, X. Kong and Y. Li, *Nat. Commun.*, 2022, **13**, 7873.

41 W. Yao, J. Chen, Y. Wang, R. Fang, Z. Qin, X. Yang, L. Chen and Y. Li, *Angew. Chem., Int. Ed.*, 2021, **60**, 23729–23734.

42 C. Dai, A. Zhang, M. Liu, X. Guo and C. Song, *Adv. Funct. Mater.*, 2015, **25**, 7479–7487.

